ACS Photonics

Article

pubs.acs.org/journal/apchd5

Broadband Terahertz Sensing on Spoof Plasmon Surfaces

Binghao Ng,[†] Stephen M. Hanham,[‡] Jianfeng Wu,[§] Antonio I. Fernández-Domínguez,[⊥] Norbert Klein,[‡] Yun Fook Liew,[∥] Mark B. H. Breese,[#] Minghui Hong,[§] and Stefan A. Maier*[,†]

[†]Department of Physics and [‡]Department of Materials, Imperial College London, South Kensington, London, SW7 2AZ, U.K.

[§]Department of Electrical and Computer Engineering, National University of Singapore, 4 Engineering Drive 3, 117576, Singapore

[⊥]Departamento de Física Teórica de la Materia Condensada, Universidad Autónoma de Madrid, E-28049 Madrid, Spain

[∥]National Metrology Centre, 1 Science Park Drive, 118221, Singapore

[#]Center for Ion Beam Applications (CIBA), Department of Physics, National University of Singapore, 2 Science Drive 3, 117542, Singapore

Supporting Information

ABSTRACT: In this paper, we show that broadband spectral data can be experimentally extracted from corrugated metallic surfaces consisting of a linear array of subwavelength grooves supporting tightly confined spoof plasmons. Using a combination of the scattering edge coupling method and short-time Fourier transform, we are able to discern the group velocity characteristics of a spoof plasmon pulse, which in turn allows for the extraction of broadband dispersion data from 0.4 to 1.44 THz in a single measurement. Refractive index sensing of various fluids is demonstrated at microliter volume quantities by monitoring changes in not only the dispersion relation but also the frequency-dependent attenuation of the spoof plasmons. This gives information about both the real and imaginary part of the refractive index of an analyte, indicating the potential for spoof plasmon surfaces to fully characterize substances in the terahertz regime. Lastly, we show that the strong electromagnetic field confinement near the effective spoof plasmon frequency allows for surface-enhanced absorption spectroscopy, demonstrated here with α-lactose monohydrate powder. This allows us to take a more spectroscopic approach to THz sensing whereby substances can be uniquely identified by their spectral fingerprints. The enhanced light−matter interactions that occur in the vicinity of the spoof plasmon surface allow for a more efficient use of the limited power of current terahertz sources. Together with the ability to integrate spoof plasmon surfaces with microfluidics and to freely design its electromagnetic properties, we believe that these surfaces can be a very versatile platform on which chip-scale terahertz sensing can be performed.

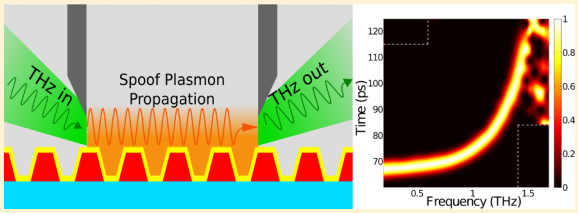

KEYWORDS: *metamaterials, sensors, plasmonics, THz, subwavelength materials*

Terahertz (THz) radiation, loosely defined as electromagnetic waves with frequencies between 0.1×10^{12} and 10×10^{12} Hz, holds great promise in biological and security sensing applications.[1−6] This is because THz radiation is nonionizing and many complex molecules have rotational and vibrational modes in the THz frequency band. However, the size mismatch between the photon wavelength and the sensed analyte size and a lack of powerful sources hamper the progress of THz technology toward more widespread real-world applications.[7,8] Consequently, researchers have turned to metamaterials, which offer unprecedented control of light, in an attempt to address some of the challenges of THz research.[9−13] In particular, spoof plasmons, which are essentially bound electromagnetic surface modes, offer a surprisingly easy way to confine light to subwavelength scales on corrugated perfect electrical conductor (PEC) surfaces.[14,15] This tight confinement of light cannot be supported by conventional unstructured metal−dielectric interfaces at low frequencies.[16] Hence, this means that corrugated surfaces supporting spoof plasmons, which we simply term spoof plasmon surfaces (SPSs), can potentially enhance light−matter interactions as well as allow small sample volumes to be sensed even in the lower frequency regimes of the electromagnetic spectrum. Furthermore, the optical properties of SPSs can be easily engineered through the geometrical parameters of the corrugations, allowing SPSs to be applied to sensing applications from the gigahertz (GHz) to mid-IR frequencies. SPSs with different geometries have been experimentally demonstrated and widely studied for a range of wave-guiding functionalities.[17−21] In the microwave regime, corrugated surfaces have also been used extensively for low-loss waveguides and high-performance feed antennas.[22] However, very little scientific effort has been devoted to the exploitation of these novel structures to overcome problems in THz sensing.[23−25]

Recently, we experimentally demonstrated high-performance narrowband refractive index sensing on a SPS using an Otto prism configuration,[23] much like surface plasmon polariton

Received: July 26, 2014
Published: September 2, 2014

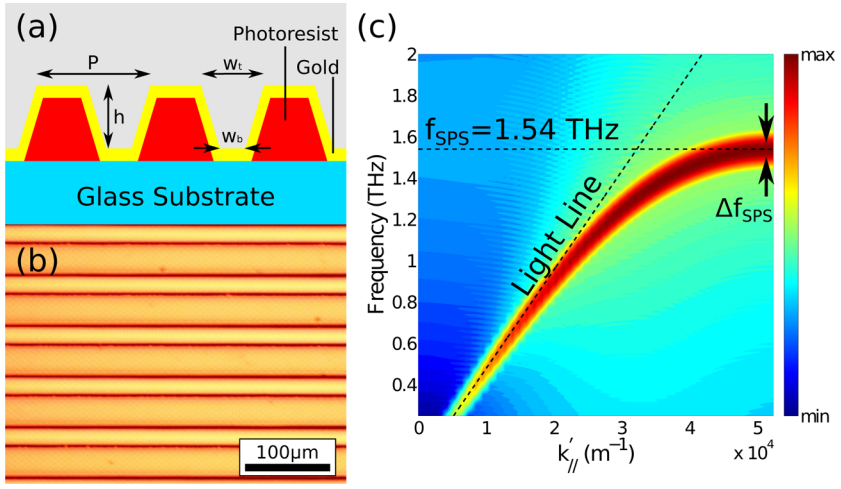

Figure 1. (a) Schematic diagram of SPS with P = 60 μm, h = 31 μm, w_t = 37 μm, and w_b = 25 μm. The thickness of gold is 600 nm. (b) Optical microscope image of SPS fabricated by photolithography. (c) Calculated band structure of SPS. The width of the spoof plasmon mode at the Brillouin zone edge, Δf_{SPS}, gives an estimate of the lifetime of the spoof plasmon; $1/\Delta f_{SPS} \approx 20$ ps.

sensing at visible frequencies.[26] Here, we take spoof plasmon THz sensing one step further by showing that broadband information regarding the spoof plasmon propagation on SPSs can be extracted using a combination of the scattering edge coupling scheme[17,27] and short-time Fourier transform (STFT). Notably, the dispersion of the spoof plasmons can be extracted with a single measurement, and only two measurements are needed to retrieve the corresponding attenuation coefficient. This allows for quick acquisition of data with minimal sample processing. To demonstrate broadband refractive index sensing, various fluids are sensed at microliter volumes and variations in the dispersion of the spoof plasmons and the attenuation coefficients are shown. Lastly, we show that SPSs can potentially be used to identify substances with absorption peaks within the operating spectral window of the SPS. In particular, we deposit a thin layer of α-lactose monohydrate with an absorption peak at 1.37 THz on our SPS and show that the confined fields of the spoof plasmons lead to greater sensitivity to this absorption peak, similar to surface-enhanced sensing in the optical and near-IR frequency regimes. This means that we can potentially take a spectroscopic approach to sensing with SPSs, where there is the opportunity to uniquely identify substances in addition to simply detecting refractive index changes. The versatility of SPS sensors, which can be designed for narrowband and broadband operation, together with its flexibility to be integrated with microfluidics and surface functionalization could bring THz sensing one step closer to real-world applications.

RESULTS AND DISCUSSION

SPS Design and Fabrication. Our SPS, which is designed to work between 0.2 and 2 THz, consists of a linear array of subwavelength grooves as shown in Figure 1a. This structure supports tightly confined, TM-polarized spoof plasmons.[23,28] The grooves are fabricated via conventional UV photolithography of a positive photoresist followed by the deposition of a 600 nm layer of gold directly on top via sputtering. The photoresist and gold layers are depicted as the red and yellow regions, respectively, in Figure 1a. The final structure closely resembles a corrugated perfect electrical conductor surface, as the gold layer is much thicker than the skin depth of gold at THz frequencies. As a result, the THz radiation does not interact with the photoresist beneath the gold layer. The grooves have a period P = 60 μm, a depth h = 31 μm, a top width w_t = 37 μm, and a bottom width w_b = 25 μm (see Figure 1a). Figure 1b shows an optical microscope image of the fabricated SPS. The subwavelength nature of the grooves means that the SPS operates in the *metamaterial* regime, where electromagnetic radiation is not sensitive to the individual corrugations but experiences an effective medium instead. An alternative way of describing the SPS when the period is much smaller than the wavelength is via the effective surface impedance approximation.[29] Figure 1c shows the dispersion relation of the SPS calculated with Lumerical FDTD Solutions (see Methods). At higher frequencies, the dispersion deviates from the light line, indicating a strong confinement of the THz fields normal to the SPS. Moreover, it can be seen that within the frequency range of interest, which is 0.2 to 2 THz, there is only one bound mode supported on this SPS. The spoof plasmon frequency saturates at f_{SPS} = 1.54 THz, representing the cutoff frequency of the SPS as shown in Figure 1c.

Scattering Edge Coupling to Spoof Plasmons. Spoof plasmons, being bound surface waves, cannot be directly coupled to from free-space propagating light due to frequency and momentum conservation. Here, we use a scattering edge coupling method to phase match the incident THz radiation to the tightly bound spoof plasmons and show that broadband dispersion data can be extracted in a single measurement.[17,27] As shown in Figure 2a, THz radiation generated by a THz time-domain spectrometer (THz-TDS) is scattered off a sharp razor blade edge and coupled into a spoof plasmon, which propagates for a distance D. The spoof plasmon is then scattered off a second razor blade edge back into free space radiation and collected by a detector. Figure 2b shows the normalized time-domain signal when a thick gold film (red line) and the SPS (blue line) is placed in the scattering edge coupling setup. In the case of the gold film, which is approximately 200 nm thick, the time-domain signal is a very short pulse. This is because only unconfined, dispersionless, Sommerfeld–Zenneck waves propagate on an unstructured metal–dielectric interface at low frequencies.[16,27] In contrast, the signal from the SPS is much longer, indicating dispersion of the surface waves. In our experiments, a propagation distance $D \geq 8$ mm, corresponding to at least 130 periods, was used to

dx.doi.org/10.1021/ph500272n | ACS Photonics 2014, 1, 1059–1067

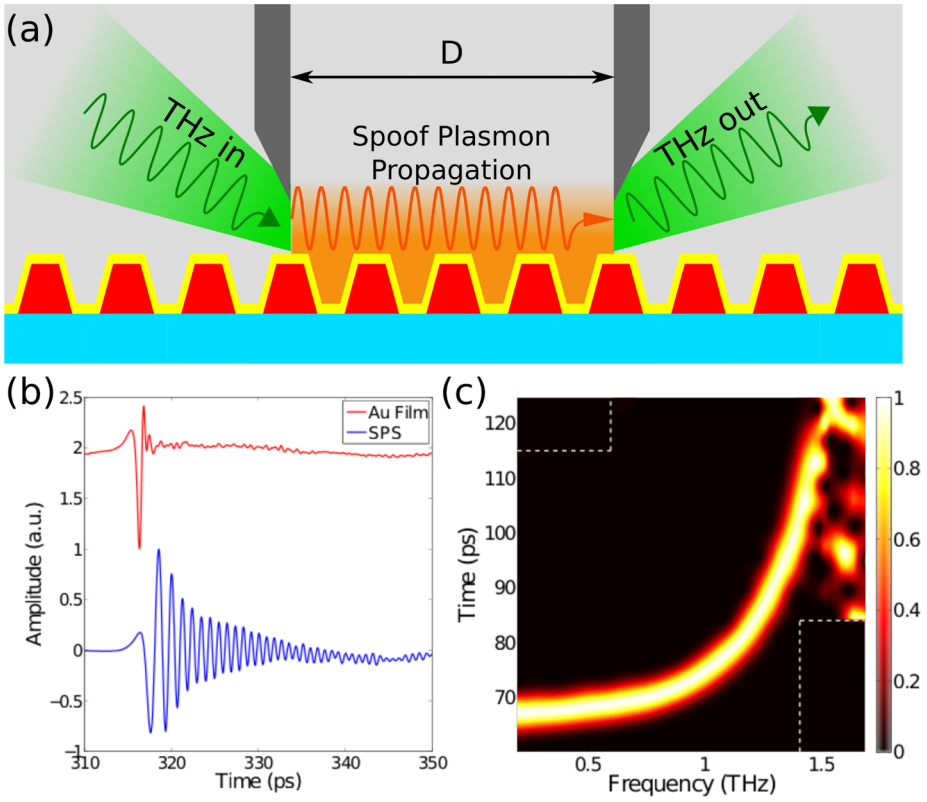

Figure 2. (a) Diagram of the scattering edge coupling configuration. (b) Scattering edge coupled time-domain signal of an Au film (red line) and SPS (blue line) with D = 8 mm. The time-domain signals are vertically displaced from each other to facilitate easy reading. (c) Filtered spectrogram of SPS with D = 8 mm. The time−frequency filters demarcated by the white dashed lines are applied by setting the enclosed region to zero in order to filter out any signal that is not from the spoof plasmons and improve the visibility of the actual spoof plasmon time−frequency curve.

ensure that the excited spoof plasmon frequency components have enough time to be properly separated from each other by the time they reach the second razor blade.

The time-domain data collected from the scattering edge coupled spoof plasmon were analyzed with STFT[30] (see Methods). This technique allows us to analyze the frequency content of the time-domain signal at each point in time by imposing a sliding time window on the raw time-domain data. The resulting data constitute a time−frequency plane called a spectrogram. In other words, the spectrogram provides us with a description of the frequency components of the spoof plasmon arriving at the second razor blade after propagating a distance D at any particular time. This information enables us to obtain the group velocities of the spoof plasmons propagating on the SPS and subsequently extract their dispersion relation (see Methods). Figure 2c shows the SPS spectrogram, $\overline{S}_{norm}$, with D = 8 mm, which is normalized to the maximum amplitude at each frequency. The first feature to note is the main curve in the center of the spectrogram extending approximately from 68 to 120 ps in time and 0.2 THz to approximately 1.5 THz in frequency. This gives the times, τ, and the respective frequencies, ω, at which most of the electromagnetic energy carried by the spoof plasmons arrives at the second razor blade. Also, the amplitude of the spoof plasmon signal, $A(\omega, \tau)$, can be obtained from the unnormalized spectrogram, $\overline{S}$. This quantity can be used to calculate the attenuation experienced by the spoof plasmon as it propagate on the SPS, as shall be seen later.

From Figure 2c, it is clear that the different frequency components of the spoof plasmon pulse take different amounts of time to travel the distance D, and hence the group velocity is strongly frequency dependent. For example, the 0.5 THz frequency component arrives at 68 ps, while that of 1.4 THz arrives around 32 ps later. Note that the time value is relative to the start point from which the time-domain data are collected and is not indicative of how much time the spoof plasmon takes to travel the distance D. It is the *difference* in the time taken that is important here, as it tells us the difference in group velocities between different frequency components of the spoof plasmon pulse.

Time-frequency filtering is employed by setting the amplitude of the spectrogram to zero within specific time−frequency windows in order to improve the visibility of the spoof plasmon curve. These are required due to contributions to the raw time-domain data from light that is not coupled into spoof plasmons as well as secondary reflections that occur between the razor blades (see Figure S1 in the Supporting Information). By filtering out the extraneous data, we can clearly pick out the signal due to the spoof plasmons propagating on the SPS. The white dashed lines in Figure 2c demarcate the area in which the time−frequency filters are applied. The lowest frequency maxima at each time point on the spectrogram are picked out, resulting in a series of time−frequency coordinates, (τ_i, ω_i), from which we are able to calculate the dispersion relation of the spoof plasmons as shown in Figure 3. The method employed to extract the real part of the parallel component of the modal wave-vector, $k'_{\parallel}$, from (τ_i, ω_i) is detailed in the Methods section, and the smallest frequency separation between data points is 16 GHz, as given by the STFT. Note that the complex parallel

dx.doi.org/10.1021/ph500272n | ACS Photonics 2014, 1, 1059−1067

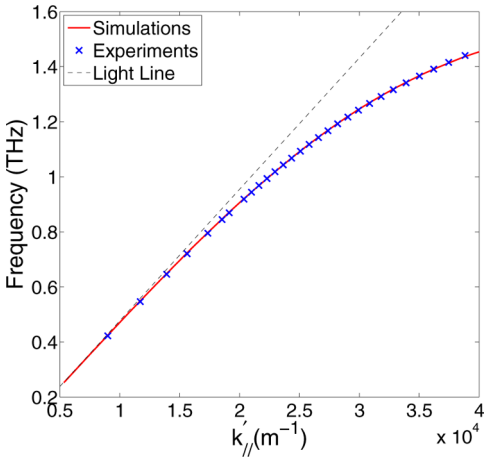

Figure 3. Simulated (red solid line) and experimentally extracted (blue crosses) SPS dispersion relation. The light line is given by the black dashed line.

component of the wave vector is defined as $k_{\|} = k'_{\|} + i\bar{\alpha}_F/2$, where $\bar{\alpha}_F$ is the power attenuation coefficient of the spoof plasmons due predominantly to the dielectric filling the grooves. We relate the lowest frequency peak at each time point to the spoof plasmon because the SPS supports only one mode in our frequency range of interest, as shown in Figure 1c. The experimentally extracted dispersion plotted as blue crosses in Figure 3 is in excellent agreement with the calculated dispersion (red solid line, extracted from the peaks of Figure 1c) and gives information about the SPS from 0.4 to 1.44 THz. We were unable to extract the dispersion relation all the way to the Brillouin zone band edge ($k'_{\|} = \pi/P = 5.24 \times 10^4$ m^{-1}). This is because as we approach the SPS cutoff frequency, $f_{SPS} = 1.54$ THz, the signal-to-noise ratio deteriorates rapidly due to a lower coupling efficiency from free-space radiation to spoof plasmons. We note here that the coupling to spoof plasmons could be made more efficient by adopting a microwave engineering approach where the SPS impedance is matched with that of an excitation transmission line. This would be an important improvement for the development of practical spoof plasmon sensors.

Using the definition of the out-of-plane confinement length,

$$L_z = (k_{\|}'^2 - k_0^2)^{-1/2} \quad (1)$$

where k_0 is the free-space wavevector, we can conclude that, at 1.4 THz, the spoof plasmon can be confined to a region as small as 43 μm normal to the SPS. This represents a field confinement of approximately $\lambda_0/5$, where λ_0 is the free-space wavelength. Thus, we can expect that light−matter interactions are drastically enhanced in this region of the SPS surface and can potentially be used for sensing applications. Meanwhile, at low frequencies such as 0.5 THz, we can see that the dispersion relation is very close to the light line (Figure 3, black dashed line), indicating poorly confined fields.

Figure 4 shows normalized spectrograms with D = 8 mm, 10 mm and 12 mm, and the appropriate time−frequency filters applied (indicated by white dashed lines). These panels show how the spoof plasmon time−frequency curve shifts to later times as the distance between the razor blades is increased. With every 2 mm increase in D, the onset of the spoof plasmon curve is delayed by approximately 6.7 ps as expected, since low-frequency spoof plasmon components travel close to the speed of light. We highlight here that each spectrogram contains information over a broad frequency range of 0.2 THz to almost 1.5 THz and is obtained by a single measurement using scattering edge coupling and STFT.

Refractive Index Sensing with SPSs. To investigate the changes in the SPS properties as its dielectric environment is modified, the grooves are filled with various fluids, namely, air (n = 1, control), diesel ($n \approx 1.45$), liquid paraffin ($n \approx 1.47$), olive oil ($n \approx 1.51$), and glycerin ($n \approx 1.85$). The fluids used here have a smoothly varying refractive index profile without sharp spectral features (see Figure S2 in the Supporting Information). The SPS grooves are filled by first covering the entire SPS with the fluids above. Excess fluid is then physically removed gently using a thin plastic sheet. Care is taken to remove any fluid on the SPS that is not in the groove. The SPS is rinsed with toluene and distilled water, and a reference measurement is taken between each fluid measurement to ensure that the SPS is clean and there is no change in the optical properties of the SPS.

Figure 5a shows how the dispersion relation is red-shifted as the real part of the refractive index of the fluids filling the grooves is increased. For example, at $k_{\|}/k_0 = 1.25$, the spoof plasmon frequencies for air, diesel, liquid paraffin, olive oil, and glycerin are 1.4, 1.19, 1.16, 1.14, and 0.99 THz, respectively. This is attributed to an increase in the effective refractive index of the SPS due to the presence of the fluids. The dispersion relations of the spoof plasmons when the SPS grooves are filled

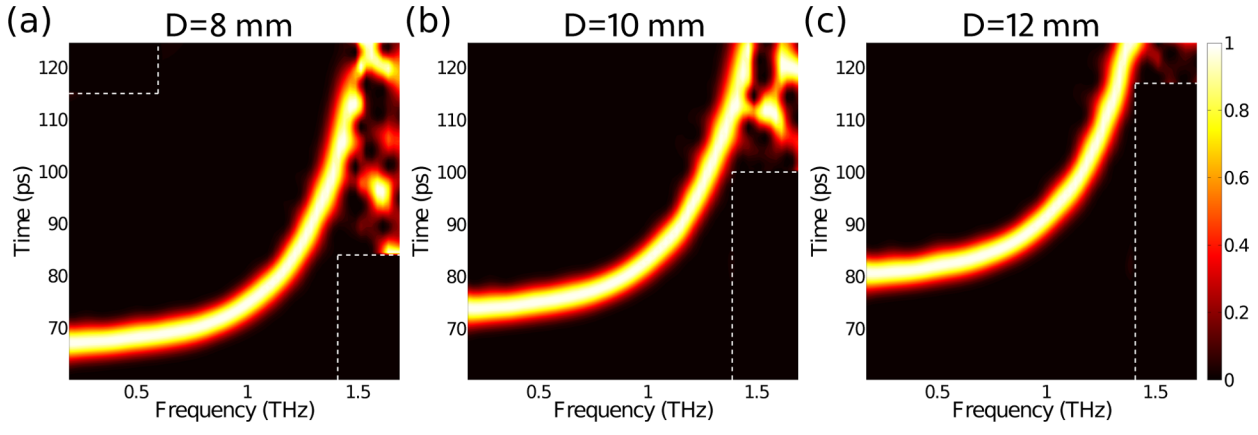

Figure 4. Spectrograms of the SPS with (a) D = 8 mm, (b) D = 10 mm, and (c) D = 12 mm.

dx.doi.org/10.1021/ph500272n | ACS Photonics 2014, 1, 1059−1067

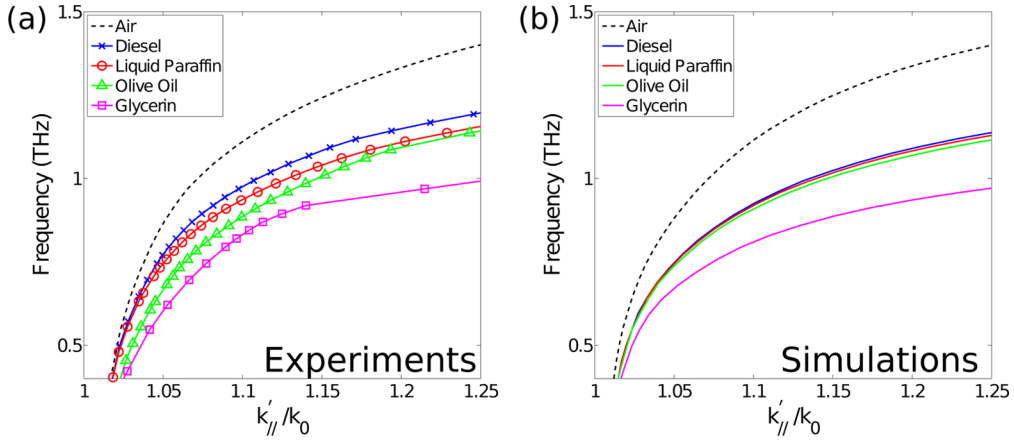

Figure 5. Dispersion of the SPS obtained from (a) experiments and (b) simulations when its grooves are filled with various fluids. The *x*-axis is normalized to the free-space wavevector k_0, to facilitate comparison of experimental and simulation results.

with various fluids, simulated with measured bulk fluid dielectric constants, are shown in Figure 5b. The experiments are well corroborated by the simulation results. The fluid refractive indices used in the simulations are extracted from transmission THz-TDS measurements using the method described by Duvillaret et al.[31] The *x*-axis in Figure 5 is plotted in units of $k'_{\parallel}/k_0$. Note that the light line in Figure 5 corresponds to a vertical line at $k'_{\parallel}/k_0 = 1$. This way, the differences between the curves are accentuated to facilitate the comparison of experimental results with simulations. This is because the real part of the refractive indices of diesel, liquid paraffin, and olive oil are very similar; hence, without the normalization of the *x*-axis, the dispersion relations would overlap and it would be hard to discern any visible differences between simulation and experiment. Likewise in Figure 3, we were unable to extract the dispersion relation all the way to the Brillouin zone edge due to a deterioration of the signal-to-noise ratio as f_{SPS} is approached. This problem is aggravated when we take into account losses due to the fluid absorption.

While being able to obtain the broadband dispersion of the spoof plasmons in one measurement allows us to detect refractive index changes in the grooves, we would ideally like to fully characterize the dielectric properties of the fluids filling the SPS grooves by accessing information about the imaginary part of the refractive indices. This can be obtained by comparing the amplitude of the spoof plasmon arriving at the second razor blade over two separate D values, namely, D = 8 mm and D = 12 mm. Straightforwardly, the power attenuation coefficient of the spoof plasmons can be written as

$$\alpha_F^{SPS} = -\ln(|A(\omega)_{D=12mm}|^2/|A(\omega)_{D=8mm}|^2)/\Delta D \qquad (2)$$

where the subscript F denotes the fluid in the groove, ΔD is the difference in the two D values (4 mm in our case), and $A(\omega)$ is the amplitude of the spoof plasmon peak in the unnormalized spectrogram $\overline{S}$, at ω. Note that α_F^{SPS} represents the attenuation of the spoof plasmon caused by the fluids and the SPS itself. Losses from the SPS are predominantly caused by increased scattering from spoof plasmons to free-space radiation due to surface imperfections as well as ohmic losses. Therefore, in order to isolate the influence of fluid absorption on the spoof plasmon propagation, the intrinsic SPS attenuation with air filling the grooves, α_{Air}^{SPS}, is subtracted from the attenuation coefficients of the other fluids to give the propagation loss due to the fluids, $\overline{\alpha}_F = \alpha_F^{SPS} - \alpha_{Air}^{SPS}$, where the subscript F now represents the fluids with the exception of air. This experimentally accessible magnitude gives us a quantitative measure of the absorptive character of the target fluids. The spoof plasmon attenuation with air as the dielectric, α_{Air}^{SPS}, is around 0.5 cm^{-1} from 0.4 to 0.9 THz. We note that the intrinsic SPS loss could increase due to an increase in metallic losses as a result of stronger field confinement. However, we found from complex eigenfrequency calculations for the SPS that increases in intrinsic SPS losses as the SPS grooves are filled with lossless dielectrics with n = 1 to 2 are small compared to $\overline{\alpha}_F$. This is why we can attribute $\overline{\alpha}_F$ mainly to fluid loss. Nonetheless, we stress that metallic losses can be a non-negligible factor when dealing with very high field confinements or fluids with high refractive indices and very low loss.

Figure 6a shows $\overline{\alpha}_F$ plotted over a frequency range of 0.4 to 0.9 THz. Comparing Figure 6a to the imaginary parts of the refractive indices of the fluids, n'', shown in Figure S2b in the Supporting Information, we can immediately see that $\overline{\alpha}_F$ follows a similar trend to the actual fluid parameters, with glycerin having the highest loss, followed by olive oil, diesel, and liquid paraffin. As can be seen in Figure 6a, the $\overline{\alpha}_F$ of the various fluids are very close to each other at 0.4 THz. This is because at low frequencies the fields on the SPS are unconfined and hence are not very sensitive to refractive index changes. On the other end of the spectrum, at 0.9 THz, we can see a marked difference in the $\overline{\alpha}_F$ values due to the increased field confinement at higher frequencies. Even for liquid paraffin and diesel, which have similar n'' values, the difference in $\overline{\alpha}_F$ is apparent at 0.9 THz. Additionally, if we look at Figure 5, we see that the difference in dispersion between diesel, liquid paraffin, and olive oil is very small due to the small differences in the real part of the refractive index among the three fluids. However, when we look at the losses they induce on the spoof plasmons, we can easily tell the difference between the three fluids. The ability to obtain loss information provides us with an additional avenue in which different substances that may have similar real parts of the refractive index can be distinguished from each other.

Figure 6b shows the simulated power attenuation coefficient of the spoof plasmons, $\overline{\alpha}_F^{Calc}$, when the grooves are filled with the various fluids. A spoof plasmon pulse is excited on a 2D array of grooves with the same dimensions as our SPS via a TM-polarized dipole source with a frequency range of 0.1 to 2 THz in Lumerical FDTD Solutions. The resultant time-domain

dx.doi.org/10.1021/ph500272n | ACS Photonics 2014, 1, 1059−1067

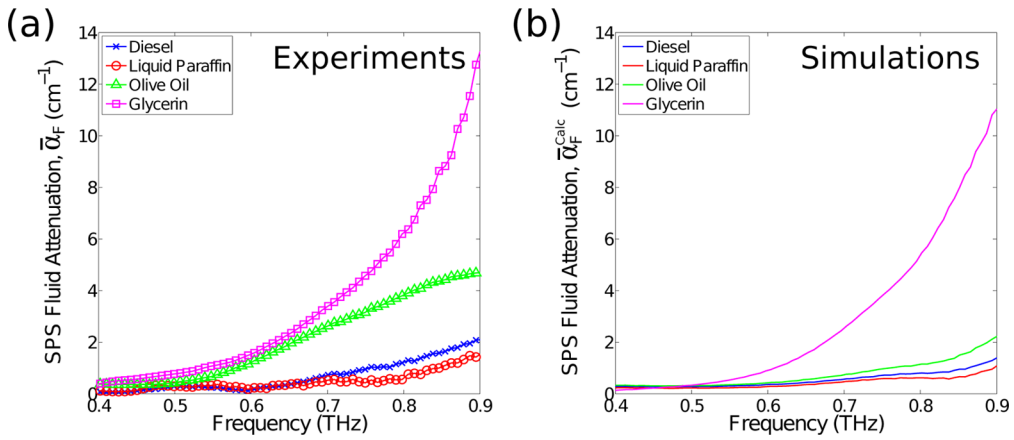

Figure 6. Attenuation coefficients of the spoof plasmon due to fluids obtained from (a) experiment, $\bar{\alpha}_F$, and (b) simulation, $\bar{\alpha}_F^{Calc}$.

data are then collected by two point monitors at a distance of 8 and 12 mm from the dipole and processed in exactly the same way as the experimental data for the various fluids. As can be seen, the behavior of $\bar{\alpha}_F^{Calc}$ matches that of experiments where the SPS is more sensitive to the fluids at higher frequencies when there is significantly stronger field confinement.

The comparison of $\bar{\alpha}_F$ across all the fluids is done from 0.4 to 0.9 THz because the SPS response of glycerin cuts off at approximately 1 THz, as shown in Figure 5a, and the data become quite noisy near f_{SPS}. Nonetheless, we stress here that the broadband data, over a range of 0.5 THz, is obtained using only two measurements per fluid. This is advantageous compared to resonant sensing methods when it comes to identifying substances via spectroscopic features. More importantly, the fluid volume used in the case of the SPS is on the order of microliters, while the measurements of the bulk fluid dielectric constants were done using fluid volumes of the order of milliliters. For example, in the case of D = 8 mm, there are 133 grooves between the razor blades. From this, we estimate that the interaction volume between the spoof plasmon and the fluids is approximately 600 nL given that the THz beam width is around 5 mm. We expect this quantity can be further reduced with a reduction in THz beam width and a SPS design that is tailored to a specific sensing purpose. One can also see how the SPS can be integrated with microfluidics to perform high-sensitivity broadband refractive index sensing.

It is conceivable to use the SPS data to retrieve the broadband refractive index of the fluids using the coupled mode method[32] since the dispersion and attenuation coefficient are related to the refractive index of the fluids filling the grooves. However, this is nontrivial since, in general, the SPS parameters are not simply related to the real or imaginary parts of the refractive index and the electromagnetic field modes are not easily defined for our grooves with slanted walls. For instance, the propagation constant generally depends on *both* the real and imaginary parts of the refractive index of the fluid, and to understand how the fields interact with the sensed samples, we would need to be able to consider all the electromagnetic modes existing in the metallic corrugations. Retrieving the exact refractive index data analytically requires more work to be done on the theory as well as SPS structure design. An alternative approach might be to use simulation methods to precalculate the $k_{||}$ for a range of complex refractive index values. In this way, experimentally obtained $k_{||}$ values can then be easily related back to a given refractive index within the precalculated set.

Surface-Enhanced THz Absorption Spectroscopy. In the final section of the paper, we show how the enhanced field confinement on the SPS can be used to identify substances with spectral features such as absorption peaks. This is useful in the case where the substance is unknown and in small volumes; a unique spectral *fingerprint* produced from the broadband detection then allows for the identification of that substance. Here, α-lactose monohydrate, with absorption peaks at 0.53 and 1.37 THz, as shown in the inset of Figure 7, is used as the analyte.[33,34] A thin layer of α-lactose monohydrate powder is deposited on the SPS by uniformly dispersing the powder via compressed air in a chamber and allowing it to settle on the SPS over 5 min. We estimate the surface mass density of the lactose powder to be approximately 300 ng/mm^2 by weighing the sample before and after the deposition.

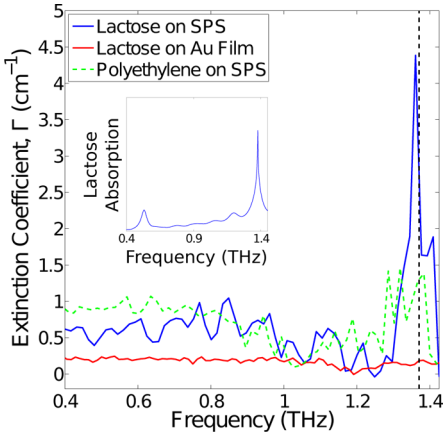

Figure 7. Γ spectra for α-lactose monohydrate deposited on SPS (blue solid line) and Au film (green dashed line) and polyethylene powder deposited on SPS (red solid line). (Inset) Absorption spectrum of α-lactose monohydrate.

The Fourier transform spectrum of the SPS time-domain signal with the lactose powder was normalized to that without the lactose powder so as to give the power transmission spectrum across the SPS, T^{SPS}. The extinction coefficient, Γ, is then given by

$$\Gamma = -\ln(T^{SPS})/D \quad (3)$$

dx.doi.org/10.1021/ph500272n | ACS Photonics 2014, 1, 1059−1067

where Γ tells us how much energy from the spoof plasmons is lost due to the presence of the lactose powder on the SPS.

For the lactose sensing measurements, D was kept constant at 10 mm and care was taken to make sure that any secondary reflections between the razor blades were not recorded in the time-domain signal. The reason that a simple Fourier transform was used instead of the STFT is because STFT tends to smear out sharp changes in the amplitude of the signal due to the application of the sliding time window. An examination of the unfiltered normalized spectrogram shows that most of the energy at 1.37 THz is coupled into spoof plasmons (see Figure S3 in the Supporting Information). Hence any spectral features observed in the Fourier transform is due to the spoof plasmons.

The blue solid line in Figure 7 shows the Γ spectrum of the α-lactose monohydrate on the SPS. The black dashed line demarcates the absorption peak of α-lactose monohydrate at 1.37 THz. As can be seen, there is a sharp peak in Γ at 1.36 THz, which we conclude is due to the absorption of the lactose powder on the SPS, taking into account the 16 GHz frequency resolution of the THz-TDS. We believe that this can be improved by using a measurement method with a higher spectral resolution such as a frequency-domain THz spectrometry or using an SPS of a different geometry, which allows for the measurement of a longer time pulse. The absorption peak at 0.53 THz is not seen due to the lack of field confinement at lower frequencies for our SPS. To further show that the Γ peak is due to enhanced light−matter interactions between the spoof plasmon and the lactose on the SPS, we performed the same measurements with α-lactose monohydrate powder deposited on a flat gold film as well as polyethylene powder deposited on the SPS. Similar surface mass densities of lactose and polyethylene powders were deposited in order to make the comparisons reliable.

We can see that the Γ spectrum for α-lactose monohydrate deposited on a flat gold film (Figure 7, red solid line) is featureless. This is because the fields on the flat gold film are very poorly confined, and thus the lactose powder does not interact with the THz radiation as much as on the SPS. To further ascertain that the peak at 1.37 THz is indeed due to the presence of lactose, polyethylene powder, which has no absorption peaks, is deposited on the SPS. The corresponding Γ spectrum is shown in Figure 7 by the dashed green line and is also featureless as expected.

We also note that the baseline value of Γ for lactose deposited on the Au film at around 0.2 cm^{-1} is lower than that of both the lactose and polyethylene powder SPS cases, with baseline Γ values between 0.5 and 1 cm^{-1}. This is attributed to the greater sensitivity of confined fields on the SPS to surface perturbations. The powder particles can act as scatterers, out-coupling spoof plasmons to free-space radiation. Furthermore, the Γ spectra for the SPS cases seem more noisy than that of the Au film due to a lower signal-to-noise ratio in the SPS cases. Nonetheless, the above three measurements show that the peak is indeed due to the presence of the α-lactose monohydrate powder, which is enhanced by the tight field confinement on the SPS.

CONCLUSIONS

In this work, we have used the concept of spoof plasmons to address some of the challenges to THz technology, namely, the lack of powerful sources and a lack of field confinement. In particular, we have shown that SPSs can be a very versatile platform for broadband THz sensing, on which we have demonstrated both refractive index sensing and surface-enhanced absorption sensing facilitated by the subwavelength field confinement on SPSs.

Lastly, we would like to point out that every sensor needs to be tailored to its specific application. There is no *one-size fits all* solution. In this paper, we have showcased the potential of the SPS for THz sensing by using an SPS with a generic design and subjecting it to a broad range of sensing parameters and scenarios. However, we note that the performance of spoof plasmon sensors can be drastically improved if they are tailored to a specific problem. A comprehensive characterization of the spoof plasmon sensing technique, its optimization, and the comparison to other well-established methods, such as THz transmission spectroscopy, are out of the scope of this paper and can be performed in the future. The myriad of SPS geometries gives engineers enormous flexibility to design solutions to sensing problems over a broad range of frequencies. Together with the possibility of integrating microfluidics and surface functionalization, we believe that SPSs are truly versatile platforms on which to bring THz sensing and all its potential benefits closer to mainstream application.

METHODS

SPS Band Structure Calculations. The band structure of our SPS was calculated using the commercial software Lumerical FDTD Solutions. The unit cell consists of a 2D groove with the same dimensions as our SPS as well as Floquet periodic boundary conditions. The spoof plasmons are excited using TM-polarized dipole sources with a frequency range of 0.1 to 2 THz placed in the near field of the groove. Time-domain data, collected by a point monitor (also in the near field of the groove), are then apodized with a Gaussian time window so that the start of the signal, corresponding to light not coupled into surface modes, is removed. The remaining time-domain signal are due to long-lived eigenmodes (i.e., spoof plasmons) and is Fourier transformed to give the frequency of the spoof plasmon for a given phase difference across the unit cell. The entire band structure can then be calculated by sweeping the phase difference across the unit cell. The width in the band diagram is a result of the FDTD method of calculation.

SPS Fabrication. A thick layer of AZ9620 positive photoresist was coated onto a glass substrate via a two-step spin-coating process. The first layer of AZ9620 was spun at 1350 rpm for 1 min followed by a soft bake at 110 °C for 80 s. The second AZ9620 layer was spin coated at the same spin speed followed by a soft bake at 110 °C for 180 s. The SPS, consisting of a linear array of subwavelength grooves, with an overall area of 25 mm × 40 mm was then patterned on the photoresist via conventional UV photolithography (Karl Suss, MA8/BA6). A 600 nm thick layer of gold was sputtered onto the photoresist (AJA International Inc., ATC 1800 V) to give the final metalized array of subwavelength grooves.

Scattering Edge Coupling to Spoof Plasmons. The Teraview Spectra 3000 THz time-domain spectrometer was used in this work for the characterization of the SPS. The gap between the razor blades and the SPS was 60 μm (250 μm in the case of the flat Au film). The THz radiation was incident on the razor blade edges at an angle of 30° from the SPS surface. The spectrometer frequency resolution was 16 GHz.

Time−Frequency Analysis of SPS Data. Short-time Fourier transform is defined by

$$S(\tau, \omega) = \int_{-\infty}^{\infty} s(t)\, w(t-\tau) e^{-i\omega t}\, dt \tag{4}$$

where $s(t)$ is the time-domain signal, $w(t)$ is the window function, and $S(\tau, \omega)$ is the STFT at time τ. The spectrogram, $\overline{S}$, is defined as $|S(\tau, \omega)|^2$. As τ is varied, $w(t-\tau)$ slides along $s(t)$ to give the STFT and

dx.doi.org/10.1021/ph500272n | ACS Photonics 2014, 1, 1059−1067

hence the frequency content of $s(t)$ within $w(t)$ at different time points.

A 20 ps Blackman−Harris minimum four-term window was used and advanced in 0.6 ps steps along the raw time-domain signal. The length of the time window is decided by looking at the width of the mode, Δf_{SPS}, at the Brillouin zone edge (see Figure 1c). The lifetime of the spoof plasmon is given by $1/\Delta f_{SPS}$ and estimated to be approximately 20 ps.

The spectrogram is normalized to the maximum magnitude at each frequency, ω_i, over all τ values, so as to remove the inherent spectral distribution of the input THz radiation, as given in eq 5.

$$\bar{S}_{norm} = \frac{|S(\tau, \omega_i)|^2}{\max(|S(\tau, \omega_i)|^2)} \quad (5)$$

Extracting SPS Dispersion. The dispersion relation of the SPS can be extracted from the time−frequency peaks of the spectrogram, (τ_n, ω_n), by looking at the time difference, $\Delta\tau_{n,n-1}$, between neighboring angular frequencies, ω_n and ω_{n-1}, iteratively. Since the distance traveled, D, is constant, $\Delta\tau_{n,n-1}$ is the result of the difference between the group velocities of spoof plasmons with neighboring frequencies v_n and v_{n-1}. The difference in propagation constant, $\Delta k_{\|}'^{n}$, can then be calculated using eq 6.

$$\Delta k_{\|}'^{n} = \Delta\omega_n\left(\frac{\Delta\tau_{n,n-1}v_{n-1} + D}{v_{n-1}D}\right) \quad (6)$$

for n = 1, 2, 3, ..., where $\Delta\omega_n = \omega_n - \omega_{n-1}$ and $\Delta\tau_{n,n-1} = \tau_n - \tau_{n-1}$.

The actual propagation constant of the spoof plasmon at ω_n is then given by eq 7.

$$k_{\|}'^{n} = k_{\|}'^{n-1} + \Delta k_{\|}'^{n} \quad (7)$$

where $k_{\|}'^{n-1}$ is the propagation constant of the previous frequency, ω_{n-1}.

The starting point of the above procedure is decided by comparing the time taken to travel D on the SPS, τ_0, to the same time taken on a flat metal surface, τ_{PEC}, by a low-frequency spoof plasmon with frequency ω_0. The group velocity of ω_0, v_0, is then given by

$$v_0 = c_0 - \frac{D(\tau_0 - \tau_{PEC})}{\tau_0\tau_{PEC}} \quad (8)$$

where c_0 is the speed of light in a vacuum. It is assumed here that ω_0 is sufficiently low such that the group velocity is linear in the vicinity of ω_0 and the propagation constant is simply given by $k_{\|}'^{0} = \omega_0/v_0$. The values of v_0 obtained using eq 8 agrees with that calculated from Figure 4 by looking at the time taken for a low-frequency spoof plasmon to propagate a given distance.

■ ASSOCIATED CONTENT

Supporting Information

Spectrograms illustrating the effects of time−frequency filtering and the deposition of α-lactose monohydrate on the SPS are shown in the Supporting Information. The refractive indices of the fluids used in the experiments are also given. This material is available free of charge via the Internet at http://pubs.acs.org.

■ AUTHOR INFORMATION

Corresponding Author

*E-mail: s.maier@imperial.ac.uk.

Notes

The authors declare no competing financial interest.

■ ACKNOWLEDGMENTS

This work was sponsored by the U.K. Engineering and Physical Sciences Research Council (EPSRC), the Leverhulme Trust, ONR Global, and the U.S. Army Transatlantic Research office. J.F.W. and M.H.H. are sponsored by the National Research Foundation, Prime Minister's Office, Singapore, under its Competitive Research Program (CRP Award No. NRF-CRP10-2012-04). B.N. expresses gratitude to the A*STAR-Imperial Partnership Program for its support.

■ REFERENCES

(1) Miles, R. E., Zhang, X.-C., Eisele, H., Krotkus, A., Eds. *Terahertz Frequency Detection and Identification of Materials and Objects*; Springer: Dordrecht, The Netherlands, 2007.

(2) Dexheimer, S. L., Ed. *Terahertz Spectroscopy: Principles and Applications*; CRC Press: Boca Raton, 2008.

(3) Taday, P. F. Applications of Terahertz Spectroscopy to Pharmaceutical Sciences. *Philos. Trans. R. Soc. A* **2004**, *362*, 351−363.

(4) Beard, M. C.; Turner, G. M.; Schmuttenmaer, C. A. Terahertz Spectroscopy. *J. Phys. Chem. B* **2002**, *106*, 7146−7159.

(5) Siegel, P. H. Terahertz Technology in Biology and Medicine. *IEEE Trans. Microwave Theory Tech.* **2004**, *52*, 2438−2447.

(6) Pickwell, E.; Wallace, V. P. Biomedical Applications of Terahertz Technology. *J. Phys. D: Appl. Phys.* **2006**, *39*, R301−R310.

(7) Siegel, P. H. Terahertz Technology. *IEEE Trans. Microwave Theory Tech.* **2002**, *50*, 910−928.

(8) Schmuttenmaer, C. A. Exploring Dynamics in the Far-Infrared with Terahertz Spectroscopy. *Chem. Rev.* **2004**, *104*, 1759−1779.

(9) Plum, E.; Fedotov, V. A.; Zheludev, N. I. Extrinsic Electromagnetic Chirality in Metamaterials. *J. Opt. A: Pure Appl. Opt.* **2009**, *11*, 074009.

(10) Reinhard, B.; Schmitt, K. M.; Wollrab, V.; Neu, J.; Beigang, R.; Rahm, M. Metamaterial Near-Field Sensor for Deep-Subwavelength Thickness Measurements and Sensitive Refractometry in the Terahertz Frequency Range. *Appl. Phys. Lett.* **2012**, *100*, 221101.

(11) Singh, R.; Al-Naib, I. A. I.; Koch, M.; Zhang, W. Sharp Fano Resonances in THz Metamaterials. *Opt. Express* **2011**, *19*, 6312−6319.

(12) O'Hara, J. F.; Singh, R.; Brener, I.; Smirnova, E.; Han, J.; Taylor, A. J.; Zhang, W. Thin-Film Sensing with Planar Terahertz Metamaterials: Sensitivity and Limitations. *Opt. Express* **2008**, *16*, 1786−1795.

(13) Wu, J. F.; Ng, B.; Turaga, S. P.; Breese, M. B. H.; Maier, S. A.; Bettiol, A. A.; Moser, H. O. Free-Standing Terahertz Chiral Meta-Foils Exhibiting Strong Optical Activity and Negative Refractive Index. *Appl. Phys. Lett.* **2013**, *103*, 141106.

(14) Pendry, J. B.; Martín-Moreno, L.; Garcia-Vidal, F. J. Mimicking Surface Plasmons with Structured Surfaces. *Science* **2004**, *305*, 847−848.

(15) de León-Pérez, F.; Brucoli, G.; García-Vidal, F. J.; Martín-Moreno, L. Theory on the Scattering of Light and Surface Plasmon Polaritons by Arrays of Holes and Dimples in a Metal Film. *New J. Phys.* **2008**, *10*, 105017.

(16) Goubau, G. Surface Waves and Their Application to Transmission Lines. *J. Appl. Phys.* **1950**, *21*, 1119−1128.

(17) Williams, C. R.; Andrews, S. R.; Maier, S. A.; Fernández-Domínguez, A. I.; Martín-Moreno, L.; García-Vidal, F. J. Highly Confined Guiding of Terahertz Surface Plasmon Polaritons on Structured Metal Surfaces. *Nat. Photonics* **2008**, *2*, 175−179.

(18) Williams, C. R.; Misra, M.; Andrews, S. R.; Maier, S. A.; Carretero-Palacios, S.; Rodrigo, S. G.; Garcia-Vidal, F. J.; Martin-Moreno, L. Dual Band Terahertz Waveguiding on a Planar Metal Surface Patterned with Annular Holes. *Appl. Phys. Lett.* **2010**, *96*, 011101.

(19) Fernandez-Dominguez, A. I.; Martin-Moreno, L.; Garcia-Vidal, F. J.; Andrews, S. R.; Maier, S. A. Spoof Surface Plasmon Polariton Modes Propagating along Periodically Corrugated Wires. *IEEE J. Sel. Top. Quant.* **2008**, *14*, 1515−1521.

(20) Fernandez-Dominguez, A. I.; Williams, C. R.; Garcia-Vidal, F. J.; Martin-Moreno, L.; Andrews, S. R.; Maier, S. A. Terahertz Surface Plasmon Polaritons on a Helically Grooved Wire. *Appl. Phys. Lett.* **2008**, *93*, 141109.

(21) Constant, T. J.; Taphouse, T. S.; Rance, H. J.; Kitson, S. C.; Hibbins, A. P.; Sambles, J. R. Surface Plasmons on Zig-Zag Gratings. *Opt. Express* **2012**, *20*, 23921−23926.
(22) Clarricoats, P. J. B.; Saha, P. K. Propagation and Radiation Behaviour of Corrugated Feeds: Part 1 - Corrugated-waveguide Feed. *Proc. IEEE* **1971**, *118*, 1167−1176.
(23) Ng, B.; Wu, J.; Hanham, S. M.; Fernández-Domínguez, A. I.; Klein, N.; Liew, Y. F.; Breese, M. B. H.; Hong, M. H.; Maier, S. A. Spoof Plasmon Surfaces: A Novel Platform for THz Sensing. *Adv. Opt. Mater.* **2013**, *1*, 543−548.
(24) You, B.; Lu, J. A.; Liu, T. A.; Peng, J. L. Hybrid Terahertz Plasmonic Waveguide for Sensing Applications. *Opt. Express* **2013**, *21*, 1786−1795.
(25) You, B.; Peng, C. C.; Jhang, J. S.; Chen, H. H.; Yu, C. P.; Lai, W. C.; Liu, T. A.; Peng, J. L.; Lu, J. Y. Terahertz Plasmonic Waveguide Based on Metal Rod Arrays for Nanofilm Sensing. *Opt. Express* **2014**, *22*, 11340−11350.
(26) Homola, J., Ed. *Springer Series on Chemical Sensors and Biosensors*, 1st ed.; Springer: New York, 2006.
(27) Saxler, J.; Gómez Rivas, J.; Janke, C.; Pellemans, H.; Bolvar, P.; Kurz, H. Time-Domain Measurements of Surface Plasmon Polaritons in the Terahertz Frequency Range. *Phys. Rev. B* **2004**, *69*, 155427.
(28) García-Vidal, F.; Martín-Moreno, L. Transmission and Focusing of Light in One-Dimensional Periodically Nanostructured Metals. *Phys. Rev. B* **2002**, *66*, 155412.
(29) Collin, R. E. *Field Theory of Guided Waves*, 2nd ed.; Wiley-IEEE: New York, 1990; pp 708−711.
(30) Oppenheim, A. V.; Schafer, R. W.; Buck, J. R. *Discrete-Time Signal Processing*; Prentice-Hall: NJ, 1998.
(31) Duvillaret, L.; Garet, F.; Coutaz, J.-L. A Reliable Method for Extraction of Material Parameters in Terahertz Time-Domain Spectroscopy. *IEEE J. Sel. Top. Quant.* **1996**, *2*, 739−746.
(32) García-Vidal, F.; Martin-Moreno, L.; Pendry, J. B. Surfaces with Holes in Them: New Plasmonic Metamaterials. *J. Opt. A: Pure Appl. Opt.* **2005**, *7*, S97−S101.
(33) Zeitler, J. A.; Kogermann, K.; Rantanen, J.; Rades, T.; Taday, P. F.; Pepper, M.; Aaltonen, J.; Strachan, C. J. Drug Hydrate Systems and Dehydration Processes Studied by Terahertz Pulsed Spectroscopy. *Int. J. Pharm.* **2007**, *334*, 78−84.
(34) Yamauchi, S.; Hatakeyam, S.; Imai, Y.; Tonouchi, M. Terahertz Time-Domain Spectroscopy to Identify and Evaluate Anomer in Lactose. *Am. J. Anal. Chem.* **2013**, *4*, 756−762.